Journal of
Materials Chemistry A

PAPER

View Article Online
View Journal | View Issue

Cite this: *J. Mater. Chem. A*, 2024, **12**, 9055

A platinum-based photothermal polymer with intermolecular/ligand-to-ligand charge transfer for efficient and sustainable solar-powered desalination†

Miao Zhang, ‡*[a] Md. Nahian Al Subri Ivan,‡[b] Yingjie Sun,[a] Zikang Li,[a] Shuvra Saha,[b] Safayet Ahmed,[b] Huiying Liu,[a] Yidi Wang,[a] Yuen Hong Tsang *[b] and Wai-Yeung Wong *[a]

The interfacial solar steam generation (ISSG) system has garnered widespread attention in addressing the global freshwater scarcity issue. Enhancing the performance of the ISSG system relies on the development of highly efficient photothermal materials. We have developed a new platinum-based photothermal polymer, named PffBTPt, which shows excellent sunlight absorption capability through intermolecular and ligand-to-ligand charge transfer mechanisms investigated by DFT calculations. An effective and stable solar evaporator is successfully fabricated by depositing PffBTPt onto a polyurethane foam (PU) substrate. The surface temperature of PffBTPt-attached PU rapidly rises up to nearly its peak value of 66.4 °C within 1 minute under 1 sun due to effective nonradiative transitions, surpassing 36.5 °C of the PU. The solar evaporator exhibits a water evaporation efficiency of 85.6% and an evaporation rate of 1.57 kg m^{-2} h^{-1} under 1 sun, as well as achieves a 3–5 order of magnitude reduction in the concentrations of Ca^{2+}, K^+, Mg^{2+}, and Na^+ after desalination of seawater. In this study, the organometallic photothermal material is reported for the first time, demonstrating its significant potential in simultaneous clean water production and seawater desalination. This research also offers a fresh perspective on the molecular design aimed at creating effective organometallic photothermal polymers by integrating a suitable metal complex into the polymer backbone.

Received 23rd December 2023
Accepted 26th February 2024

DOI: 10.1039/d3ta07980e

rsc.li/materials-a

---

[a] Department of Applied Biology and Chemical Technology and Research Institute for Smart Energy, The Hong Kong Polytechnic University, Hung Hom, Hong Kong, P. R. China. E-mail: wai-yeung.wong@polyu.edu.hk; bjtumiao.zhang@polyu.edu.hk

[b] Department of Applied Physics, Photonic Research Institute, Materials Research Center, The Hong Kong Polytechnic University, Hung Hom, Hong Kong, P. R. China. E-mail: yuen.tsang@polyu.edu.hk

† Electronic supplementary information (ESI) available. See DOI: https://doi.org/10.1039/d3ta07980e

‡ M. Zhang and M. N. A. S. Ivan contributed equally to this work.

Miao Zhang

Dr Miao Zhang obtained her PhD degree in 2019 under the supervision of Prof. Zhang Fujun from Beijing Jiaotong University in China. Subsequently, she was selected as a postdoctoral fellow under the supervision of Prof. Wong Wai-Yeung, Raymond at the Hong Kong Polytechnic University (PolyU) through the Hong Kong Scholars Program (2019). Currently, she holds the position of Research Assistant Professor in the Department of Applied Biology and Chemical Technology at PolyU. Her research interests focus on the development of novel organic/organometallic materials for photovoltaic and photothermal application. To date, she has achieved more than 60 publications in SCI journals, which have garnered more than 4000 citations.

1. Introduction

Sunlight-clean water production from seawater, industrial wastewater, and domestic sewage is recognized as a crucial technology for sustainable development.[1–3] The interfacial solar steam generation (ISSG) system holds immense promise for the practical implementation of this technology. Conventional seawater desalination and wastewater purification systems have high energy requirements and necessitate significant investments in infrastructure establishment.[4,5] The ISSG system is electricity independent and harnesses the photothermal properties of a solar evaporator to capture sunlight and concentrate heat at the air–water interface, facilitating vapor generation effectively.[6–8] An efficient solar evaporator performs two essential functions: (i) it efficiently absorbs a broad spectrum of sunlight, converts it into heat, and localizes the heat at the site of evaporation, and (ii) continuously absorbs a controlled amount of water and transfers it to the area where heat is concentrated.[9,10] A porous substrate, such as polyurethane (PU) foam, is commonly employed in the fabrication of a solar evaporator to improve water transportation and facilitate vapor release.[11,12] Various photothermal materials have been utilized to decorate these porous substrates, enabling efficient conversion of light into heat. Plasmonic nanoparticles, including gold (Au),[13] silver (Ag),[14] and palladium (Pd),[15] are particularly popular in ISSG applications due to their strong sunlight absorption capabilities around the localized surface plasmon resonance peak. These plasmonic materials are often combined with carbon-based materials to broaden the absorption spectrum of sunlight. Carbon-based materials, known for their conjugated structure, are effective in absorbing a broad spectrum of light. Different types of carbon-based materials, such as carbon black, reduced graphene oxide (rGO), carbon nanotubes (CNTs), and carbonized biomass, have been explored as photothermal materials for ISSG applications.[16–18]

Two-dimensional (2D) materials like covalent-organic frameworks (COFs) and metal–organic frameworks (MOFs) have also been successfully employed in ISSG applications due to their highly ordered and porous structures.[19,20] Most COF and MOF materials have relatively narrow absorption windows, so they are often combined with carbon-based materials or other photothermal materials to enable solar steam generation. So far, polypyrrole (PPy) is the only one-dimensional (1D) photothermal polymer reported for ISSG application.[21,22] Z. Wang *et al.* prepared a PPy decorated wood for solar steam generation, which shows a high absorbance within a broad wavelength range (300–2500 nm), and an evaporation rate and efficiency of 1.014 kg m^{-2} h^{-1} and 72.5% under 1 sun, respectively.[23] S. Wang *et al.* produced a solar evaporator by using electrodeposited PPy on nickel foam as the top solar absorbing layer and PU sponge as the bottom water pumping layer. This setup achieved an evaporation efficiency of 82.18% under 1 sun and an evaporation rate of 1.2562 kg m^{-2} h^{-1} under 0.755 sun.[24] 1D polymers consisting of one or more monomers in the backbone present numerous advantages such as abundant raw materials, straightforward synthesis, synthetic flexibility, strong and tuneable absorption, and good thermal stability.[25–27] The further development of 1D photothermal polymer materials holds great importance for the advancement in the ISSG field. Organometallic polymers that incorporate at least one metal complex as a polymerized monomer show a great potential as next-generation 1D photothermal materials, which can combine the beneficial properties of both metal complexes and organic compounds.[28,29] Strategies such as promoting conjugation, enhancing structural planarity, and facilitating intermolecular interactions have proven effective in achieving the broad solar light absorption of organic polymers.[30,31] In contrast, metal complexes exhibit diverse mechanisms for adjusting the absorption spectra, for example, through metal-to-ligand charge transfer (MLCT), ligand-to-ligand charge transfer (LLCT), or intraligand charge transfer (ILCT), which are induced by multiple interactions among the primary ligand, auxiliary ligand, and metal center.[32–36] As mentioned earlier, maximizing sunlight absorption is imperative for the development of highly efficient photothermal materials. It would be a wise approach to develop new photothermal polymers with high light-absorbing capability by introducing the above multiple mechanisms within a single organometallic molecule.

In this study, we designed two small molecules, Pt(N,N)(O,O) and ffBT-2ET-2DT, as the polymerization monomers. These monomers were utilized to create a novel organometallic polymer, PffBTPt, through the Sonogashira coupling reaction. The resulting polymer possesses a large planar π-conjugated backbone facilitated by the alkynyl functional group as a π-bridge linker. By combining the advantages of the platinum(II)-based metal complex and electron-withdrawing organic group, the polymer exhibits excellent light absorption capability across a broad solar spectrum, particularly in the NIR region. The absorption properties were carefully investigated through absorption spectral measurement and density functional theory (DFT) calculations. To evaluate the photothermal conversion performance, an efficient solar evaporator was constructed by depositing the organometallic polymer onto PU foam using the drop casting method, referred to as OPU for convenience. The prepared OPU demonstrates a good evaporation efficiency more than 83% and an evaporation rate over 1.5 kg m^{-2} h^{-1} for both water and seawater samples under 1 sun, comparable to the reported studies. Furthermore, the OPU exhibits good operation stability during long-term and numerous cycle tests. The OPU significantly reduces the content of four metal cations, namely, Ca^{2+}, K^{+}, Mg^{2+} and Na^{+}, in seawater after desalination. The conversion of solar energy to thermal energy on the surface of OPU can be attributed to the efficient energy release through nonradiative relaxation upon exposure to sunlight across the entire evaporator. Experimental results and theoretical calculations both demonstrate the great feasibility of the PffBTPt polymer as an effective photothermal material for solar evaporation and seawater desalination. This work presents a valuable strategy for developing efficient organometallic photothermal polymers by incorporating appropriate metal complexes in the polymer backbone. Importantly, it represents the first example of utilizing an organometallic polymer for simultaneous clean water production and seawater desalination.

2. Results and discussion

2.1 Synthesis and characterization of monomers and the polymer

The organometallic polymer, PffBTPt, is meticulously designed and synthesized following the reaction routes depicted in Fig. 1a. In the initial step, the two novel monomers, Pt(N,N)(O,O) and ffBT-2ET-2DT, were synthesized using the routes illustrated in Fig. 1b and c, respectively. The final polymerization was achieved through the Sonogashira coupling reaction, conducted under moderate conditions of room temperature (RT), ensuring a product yield of over 90%. Then the polymer is purified by the Soxhlet extraction with methanol, acetone and hexane in turn. The chemical structures of all intermediates, two monomers, and the target polymer, along with the specific reaction conditions for each step, are shown in the caption of Fig. 1. The ESI† provides synthetic details and all ^{1}H NMR spectra of intermediates, as well as $^{1}H/^{13}C$ NMR and mass spectra of the two newly synthesized monomers, confirming their chemical structures.

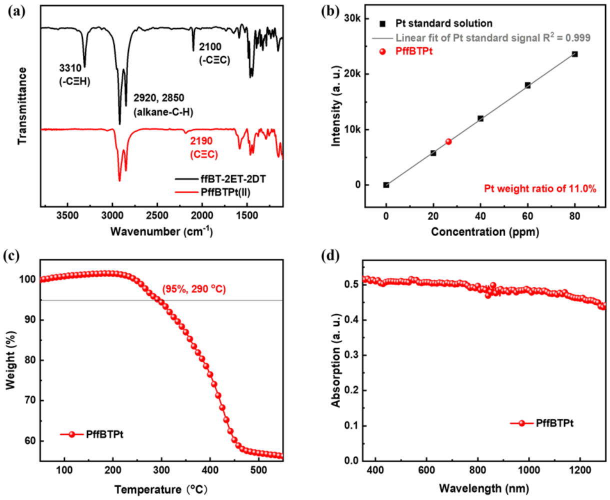

Fig. 2 (a) FTIR spectra of ffBT-2ET-2DT and PffBTPt. (b) ICP-OES curves of PffBTPt. (c) TGA and (d) DRS curves of PffBTPt.

The polymer structure is validated by the Fourier-transform infrared (FTIR) spectra of ffBT-2ET-2DT and PffBTPt shown in Fig. 2a. For ffBT-2ET-2DT, the distinctive peaks at 3310, 2920/2850, and 2100 cm^{-1} correspond to the vibration of C≡H, C–H (alkane group), and C≡C, respectively.[37] Upon successful polymerization of PffBTPt, the peak attributed to C≡H at 3310 cm^{-1} disappears. The positions of the two peaks at 2920 and 2850 cm^{-1} remain unchanged, although their intensities significantly decrease. The peak at 2100 cm^{-1} undergoes a slight redshift, and its intensity is markedly reduced, reflecting the structural modifications resulting from the enlarged conjugated polymer backbone of PffBTPt. Inductively coupled plasma optical emission spectroscopy (ICP-OES) is utilized to determine the weight ratio of the Pt component, as demonstrated in Fig. 2b. To accomplish this, PffBTPt is digested in a blend solution of HNO_3 and H_2SO_4 (1 : 1) at 100 °C overnight. A linear fit of the Pt standard solution yields a coefficient of determination of 0.999, indicating a highly accurate result.[38] The resulting Pt weight ratio is found to be approximately 11%, which closely aligns with the theoretical value. These findings, supported by the FTIR and ICP-OES results, confirm the successful synthesis of PffBTPt. The powder X-ray diffraction (PXRD) measurement in Fig. S1† indicates that the crystallinity of the resulting polymer is significantly decreased compared with that of the two small-molecule monomers due to the easily entangled polymer chain and the increased disorder in the alkyne side chain, which is consistent with the other report.[39] Only a broad peak at approximately 20° is present for the polymer, which can be attributed to π–π stacking interactions resulting from the relatively planar structure induced by the

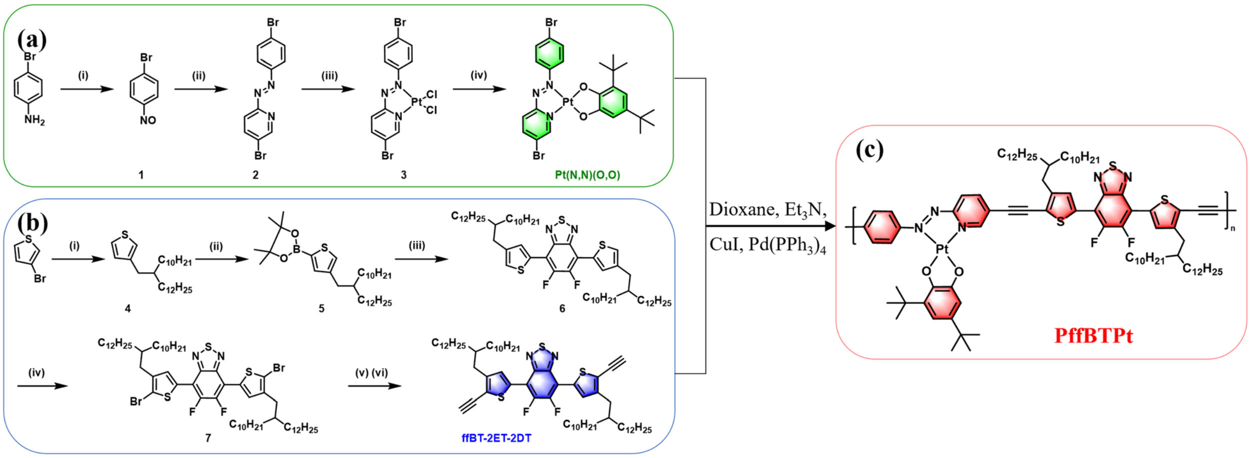

Fig. 1 The synthetic routes: (a) complex monomer Pt(N,N)(O,O): (i) DCM, aq. $2KHSO_5\cdot KHSO_4\cdot K_2SO_4$, rt. (ii) Pyrrole, 2-amino-5-bromopyridine, aq. NaOH, 90 °C. (iii) Acetonitrile: H_2O (9 : 1), K_2PtCl_4, 100 °C. (iv) DCE, 3,5-di-*tert*-butylcatechol, Na_2CO_3, 80 °C. (b) Organic monomer ffBT-2ET-2DT: (i) THF, 11-(bromomethyl)tricosane, Mg, Ni(II)Cl_2(dppp). (ii) THF, *n*-butyllithium, trimethyl borate, from −78 °C to rt. (iii) THF, 4,7-dibromo-5,6-difluoro-2,1,3-benzothiadiazole, $Pd(PPh_3)_4$, Cs_2CO_3, 60 °C. (iv) Chloroform, *N*-bromosuccinimide, rt. (v) THF, trimethylsilylacetylene, CuI, $Pd(PPh_3)_2Cl$, Et_3N, rt. (vi) THF, tetra-*n*-butylammonium fluoride. (c) Polymer PffBTPt.

rigid alkyne linker in the polymer.[40] Thermogravimetric analysis (TGA) is conducted to assess the thermal stability of PffBTPt, as depicted in Fig. 2c. The decomposition temperature (T_d) is approximately 290 °C, which corresponds to a 95% reduction in weight from the initial value. This favourable T_d value makes PffBTPt well-suited for applications as a photothermal material in solar evaporators. PffBTPt demonstrates an impressive absorption capacity that spans the wide solar spectrum from 350 nm to 1300 nm, as evidenced by UV-Vis-NIR diffuse reflectance spectroscopy (DRS) shown in Fig. 2d. The superior absorption property positions PffBTPt as a promising candidate for photothermal applications.

2.2 Density functional theory calculations

To gain a deeper understanding of the absorption mechanism of PffBTPt, the normalized absorption spectra of the two monomers in their film state were recorded, as shown in Fig. 3a. ffBT-2ET-2DT demonstrates a pronounced absorption in the UV-visible region spanning from 350 nm to 800 nm. Also, ffBT-2ET-2DT could serve as an electron-withdrawing group, enhancing the intermolecular charge transfer (ICT) effect when combined with an electron-donating unit.[41,42] On the other hand, Pt(N,N)(O,O) exhibits notable NIR absorption within the wavelength range of 800–1500 nm. DFT calculations were performed at the PBE0/def2SVP basis set to investigate the molecular geometry and energy levels of Pt(N,N)(O,O) (see Fig. 3b). The calculated highest occupied molecular orbital (HOMO) and lowest unoccupied molecular orbital (LUMO) of Pt(N,N)(O,O) are −5.26 eV and −3.97 eV, respectively. In order to further examine the electron transfer process inside Pt(N,N)(O,O) during electronic excitation, time-dependent density-functional theory (TDDFT) calculations were performed at the PBE0/def2TZVP basis set. Here, the Pt(N,N)(O,O) molecule is divided into three distinct fragments, as depicted in Fig. S2.† The interfragment charge transfer (IFCT) analysis was performed and utilized *via* the Multiwfn 3.8 dev software[43] and the results are summarized in Table S1†. The contribution of holes on fragment 2 amounts to approximately 78.4%, while the contribution of electrons on fragment 3 constitutes around 70.8%. Additionally, we observe that the electron transfer quantity from fragment 2 to fragment 3 reaches 0.555, which is the highest value among all the fragments analysed. It can be concluded that the low-energy absorption of Pt(N,N)(O,O) is primarily attributed to the LLCT characteristic, which represents one of the unique advantages of metal complexes.[44,45]

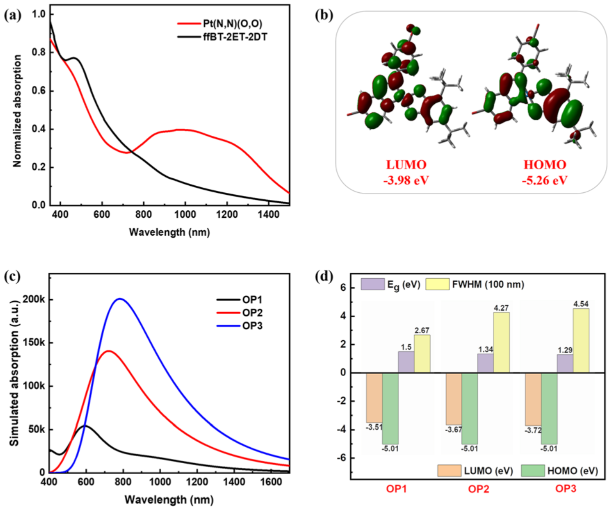

Fig. 3 (a) Absorption spectra of Pt(N,N)(O,O) and ffBT-2ET-2DT films. (b) Optimized S_0 geometry of Pt(N,N)(O,O) and the calculated LUMO and HOMO energy levels. (c) Simulated absorption spectra of OP1, OP2 and OP3. (d) Calculated LUMO, HOMO, E_g and FWHM values.

The DFT calculation of polymer structures is known to be challenging due to their large number of atoms and uncertain molecular weights.[46] To investigate the energy levels and electron transfer process of PffBTPt, we performed DFT and TDDFT calculations on three molecules with one, two, and three repeating units of PffBTPt, denoted as OP1, OP2, and OP3, respectively. Most studies have demonstrated that the long alkane chain cannot affect the energy level of the whole molecule, so we replace them with the methyl group in DFT calculations to further simplify the entire process.[47] Fig. S3† illustrates the optimized S_0 geometry of OP1, OP2, and OP3, along with their corresponding LUMO and HOMO energy levels. The optimized structures reveal that OP1, OP2, and OP3 possess planar and rigid backbones, providing a plausible explanation for the strong absorption intensity observed across a wide range of wavelengths in PffBTPt. The simulated absorption spectra of OP1, OP2, and OP3 are presented in Fig. 3c according to the TDDFT calculation. As the number of repeating units increases, the absorption intensity gradually increases, and the absorption range shifts towards longer wavelengths. Fig. 3d displays the four parameters of HOMO, LUMO, energy bandgap (E_g), and full width at half maximum (FWHM) of the simulated spectra. The HOMO/LUMO values for OP1, OP2, and OP3 are −3.51/−5.01 eV, −3.67/−5.01 eV, and −3.72/−5.01 eV, respectively. Interestingly, with an increase in the number of repeating units, the LUMO values gradually decrease while the HOMO values remain constant. The energy bandgap of OP3 molecule decreases to 1.29 eV, which correlates well with the redshifted absorption range observed. Additionally, the FWHM values of the simulated absorption spectra consistently increase for OP1, OP2, and OP3, indicating an expanded absorption range. The trend of decreasing E_g and increasing FWHM values for OP1, OP2, and OP3 highlights the strong absorption capability of PffBTPt across a broad wavelength range in the UV-Vis-NIR region.

The IFCT method was employed to analyse the electron transfer process within the OP3 molecule based on TDDFT calculation.[48,49] OP3 is segmented into four fragments, each denoted by a different colour, as illustrated in Fig. S4.† The IFCT results detailing the electron excitation from S_0 to S_1 are summarized in Table 1. The primary hole contribution, constituting 72.01%, originates from fragment 2, which is similar to the scenario observed in the monomer Pt(N,N)(O,O). The majority of electrons is dispersed between fragment 3 (45.38%) and fragment 4 (26.33%). The distribution of holes and electrons effectively clarifies the consistent HOMO values

Table 1 IFCT analysis of OP3 from TDDFT calculations of the S_0–S_1 state

	Fragment 1	Fragment 2	Fragment 3	Fragment 4
Hole (%)	2.74	**72.01**	19.20	6.05
Electron (%)	9.0	19.29	**45.38**	**26.33**
Fragment 1	0.002	0.005	0.012	0.007
Fragment 2	0.065	0.119	**0.327**	**0.210**
Fragment 3	0.017	0.037	0.087	0.051
Fragment 4	0.005	0.012	0.028	0.016

and decreasing LUMO values observed when the repeating units of PffBTPt increase as shown in Fig. 3d. The electron transfer coefficient reaches 0.327 from fragment 2 to fragment 3 and 0.210 from fragment 2 to fragment 4. Other coefficients are relatively lower and can be disregarded. OP3 not only possesses the LLCT characteristic as the monomer Pt(N,N)(O,O) but exhibits the ICT effect resulting from the donor–acceptor interactions. Therefore, the high absorption intensity of PffBTPt across the entire wavelength range is attributed to the synergistic effect of good planarity, extensive conjugation, LLCT and ICT mechanisms, which enhances the potential of PffBTPt as an effective photothermal material.

2.3 PffBTPt-based solar evaporator fabrication

The organometallic polymer PffBTPt is utilized to construct a solar evaporator, employing commercial PU as the substrate. Fig. 4a illustrates the preparation process of the OPU. PffBTPt (5 mg) was put into isopropyl alcohol (IPA) (25 mL), and the mixture was ultrasonicated for 48 hours to prepare a very dark solution. PU sponges of two different thicknesses (8 mm and 4 mm) and a diameter of 1.8 cm were washed with deionized water to remove impurities and then dried in an oven. The water in the ultrasonic chamber was regularly replaced every 2 hours to maintain the temperature between 24 °C and 38 °C. Then PU was coated with the dispersion solution by a simple drop casting method. The drop-cast PU was dried in an oven at 50 °C for 8 hours. The drop-casting and drying processes were repeated five times to prepare the OPU, which served as a PffBTPt-attached solar evaporator for subsequent photothermal applications, following the setup outlined in Fig. S5.† The particle size of PffBTPt in IPA solution was analysed using the dynamic light scattering (DLS) method on a Zetasizer Advance Range platform. The intensity-based size distribution of PffBTPt can be observed in Fig. 4b. The *Z*-average value is 256.6 nm, and the polydispersity index (PDI) is 0.261. The solar absorption capacity of both PU and OPU substrates was examined by using a UV-Vis-NIR spectrophotometer, as shown in Fig. 4c. The OPU exhibited a superior full-solar-spectrum-absorbing capability (300–2500 nm) compared to the PU substrate. These findings align well with the results from the DSC test and TDDFT calculations of PffBTPt.

The photothermal properties of PffBTPt were directly assessed by capturing thermal images of both dry PU and OPU under 1 sun irradiation, as depicted in Fig. 5a. Initially, the temperature of the PU and OPU substrates is 25 °C and 25.2 °C, respectively. Upon 1 minute irradiation, the temperature of the OPU rapidly increased to 66.4 °C, which is significantly higher than the PU's temperature of 36.5 °C during the same duration of irradiation. This observation directly demonstrates the highly efficient light-to-thermal conversion performance of PffBTPt. Under 2 minute irradiation, the temperature values are slightly increased to 36.9 °C for PU and 67.3 °C for OPU, and these temperatures remain constant even with an extended period of irradiation. In Fig. 5b, the water contact angle (WCA) images reveal the hydrophilicity of both dry PU and OPU surfaces. The OPU surface exhibited a smaller WCA value of 84.2° compared to the PU surface's value of 108.2°, indicating that the OPU is more hydrophilic than the PU. Furthermore, the scanning electron microscopy (SEM) images presented in Fig. 5c demonstrate a significant increase in the surface roughness of

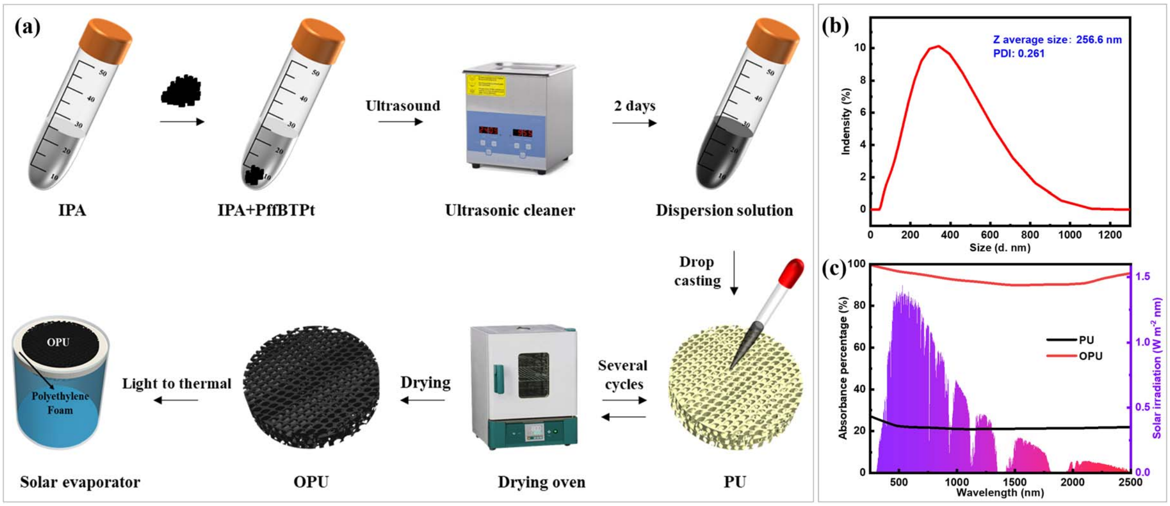

Fig. 4 (a) Preparation process of the used solar evaporator. (b) DLS curve of PffBTPt in PIA solution. (c) UV-Vis-NIR absorbance spectra of PU and OPU as well as the solar radiation spectrum.

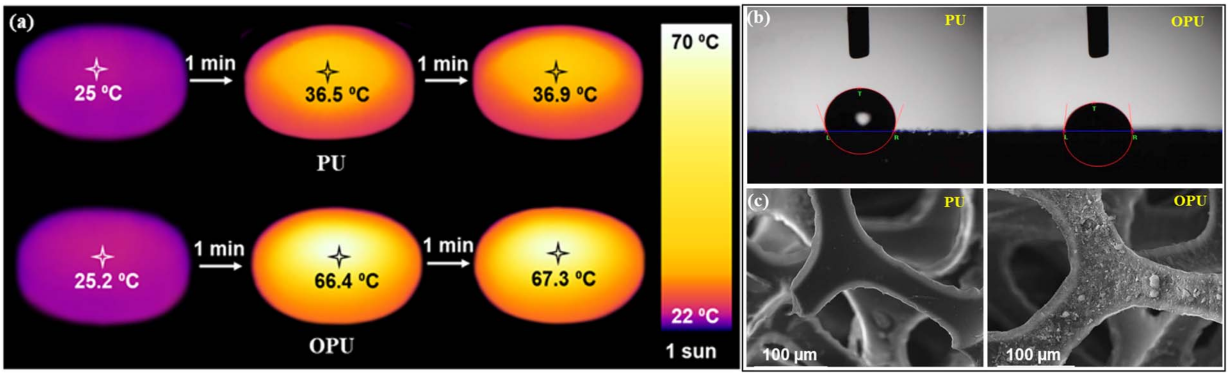

Fig. 5 Dry PU and OPU substrates: (a) thermal images before or after irradiation under 1 sun; (b) WCA photos; and (c) SEM images showing the surface morphology of PU and OPU.

the OPU due to the presence of loaded PffBTPt particles. This characteristic facilitates the promotion of water evaporation rate in the ISSG system.[21]

The photothermal mechanism of PffBTPt should stem from effective nonradiative transitions involving interconversion and vibrational relaxation processes obeying the Franck–Condon principle, which is illustrated by Femtosecond transient absorption (fs-TA) spectra. The sample for testing was prepared by dispersing PffBTPt in THF solvent with the assistance of ultrasound treatment. Fig. S6a† displays the colour fs-TA plots of the prepared solution under 800 nm excitation, with careful recording of the decay time and intensity from 830 nm to 1250 nm. The fs-TA curves at specific delay times were extracted and are shown in Fig. S6b.† The absorption intensity reaches its highest values between 830 nm and 1250 nm at 1 ps, indicating the transition of absorbed photons from the ground state to the singlet excited state.[50] After 1 ps, the excitons in the excited state return to the ground state, resulting in a gradual decrease in absorption intensity. It can be observed that all excitons return to the ground state rapidly within 500 ps. The kinetic decay curves and fitting lines at 900 nm, 1000 nm, 1100 nm, and 1200 nm are displayed in Fig. S6c–S6f.† The decay times at these four wavelengths are very fast, below 35 ps, far less than nanosecond or microsecond lifetime scales, indicating nonradiative transition processes for the excitons.[51] The kinetics show two fitted delay times of 227 fs/32.8 ps at 900 nm and 135 fs/7.2 ps at 1000 nm, which are closely related to the two nonradiative decay processes of interconversion and vibrational relaxation.[52] The considerably shorter lifetimes observed are 144 fs at 1100 nm and 118 fs at 1200 nm, suggesting highly efficient nonradiative transition of the photogenerated excitons in the longer wavelength range. The nonradiative transition typically generates thermal energy, representing the light-to-thermal conversion mechanism of the novel organometallic polymer PffBTPt. The remarkable NIR absorption of PffBTPt contributes to its highly efficient photothermal properties. The TA results prove that enhancing the absorption ability in the NIR region is an effective strategy to largely improve the light-to-thermal conversion efficiency as well as the performance of the solar evaporator.

2.4 Solar evaporation performance

To assess the performance of the prepared solar evaporators, the 8 mm thick PU and OPU samples are placed directly on top of water. The resulting mass change of water in the presence of 8 mm thick OPU is recorded and depicted in Fig. S7.† The evaporation rate of water under 1 sun is determined to be 1.10 kg m^{-2} h^{-1}, approximately 2.24 times higher than the normal evaporation rate of water (0.49 kg m^{-2} h^{-1}). The evaporation rate of water in the presence of PU is 0.66 kg m^{-2} h^{-1}, about 1.67 times lower than that of the OPU. These results clearly demonstrate that the organometallic polymer-loaded OPU could efficiently increase the water evaporation rate owing to its photothermal properties. The evaporation efficiency of the OPU is calculated to be 67.4% under 1 sun, considering its dark evaporation rate of water (0.1 kg m^{-2} h^{-1}). Detailed methods for calculating the evaporation rate and efficiency are provided in the ESI†. To enhance the evaporation rate of water, the thickness of the OPU is reduced to 4 mm to facilitate faster water transportation from the bottom to the top of the evaporator. Fig. 6a presents the mass change data of water and seawater under 1 sun, 2 sun and 3 sun, along with the corresponding evaporation rate and evaporation efficiency of the solar evaporator. The maximum evaporation rate of water in the presence of 4 mm thick OPU is measured to be 1.57 kg m^{-2} h^{-1} under 1 sun, approximately 3.18 times higher than the normal evaporation rate of water. Due to the reduced thickness, the dark evaporation rate of water is also increased to 0.3 kg m^{-2} h^{-1}. The maximum evaporation efficiency is determined to be 85.6% under 1 sun, which is 26.96% more efficient than 8 mm thick OPU. As a result, 4 mm thick OPU was selected for the subsequent experiments. The mass change rate of water from the OPU is observed under different solar irradiation levels. After 1 hour of operation under 1 sun, the mass experienced a loss of 0.40 g. Under 2 sun and 3 sun, the mass loss of water increases to 0.69 g and 0.96 g, resulting in the corresponding evaporation rate of 2.73 kg m^{-2} h^{-1} and 3.78 kg m^{-2} h^{-1}, respectively. The water evaporation efficiency exhibits a decreasing trend with the increase of solar irradiation, and the evaporation efficiency declines to 77.65% under 3 sun. The evaporation efficiency is further calculated using Gu's method considering the heat loss

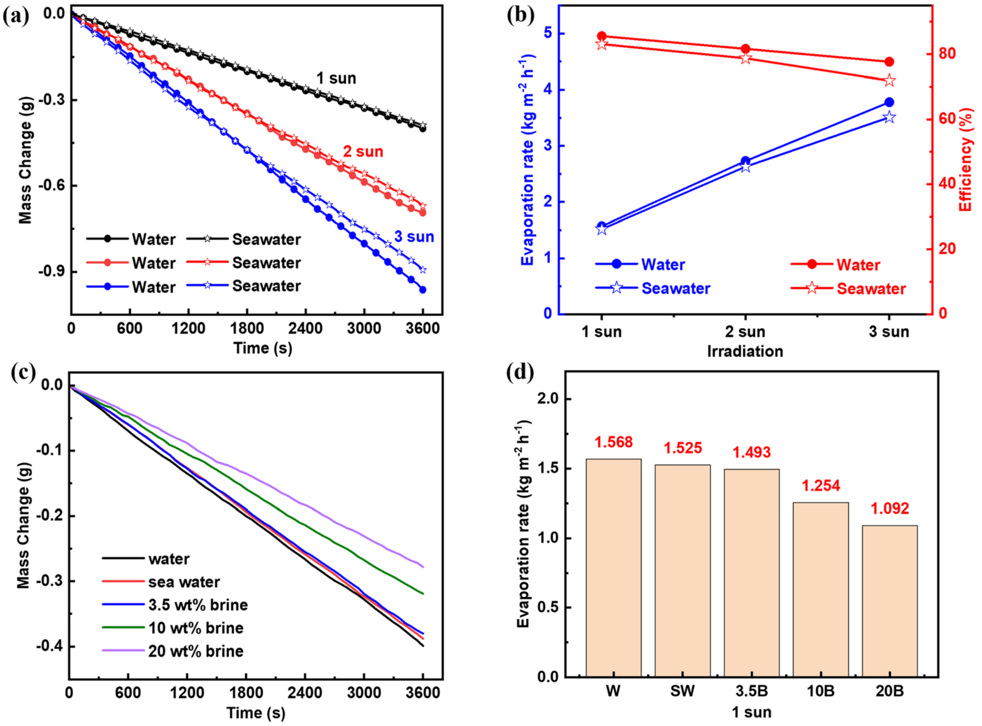

Fig. 6 (a) Mass change of water and seawater under 1 sun, 2 sun and 3 sun. (b) The corresponding evaporation rate and efficiency. (c) Mass change and (d) evaporation rate of water, seawater and brine waters under 1 sun.

as described in the ESI.†[53] The resulting solar-to-thermal and solar-to-steam efficiency are found to be 87.8% and 86.7%, respectively, which is slightly higher than the efficiency of 85.6% calculated by our method as described in the ESI.†[54]

To evaluate the seawater evaporation performance of the OPU, natural seawater with a salinity of 2.98% was collected from Shek-O beach in Hong Kong. The dark evaporation rate of seawater from the OPU is determined to be 0.29 kg m^{-2} h^{-1}. After 1 hour operation under 1 sun, the mass loss of seawater is 0.39 g, resulting in an evaporation rate of 1.52 kg m^{-2} h^{-1} and an efficiency of 83.1%, as illustrated in Fig. 6b. Probably the presence of micro-organisms and salt in natural seawater slightly reduces its evaporation rate by 3.18% under 1 sun. The mass change, evaporation rate and efficiency of seawater were also recorded for higher solar irradiation levels. Under 3 sun, the seawater evaporation rate and efficiency were observed to be 3.51 kg m^{-2} h^{-1} and 71.91%, respectively. No salt growth was observed on the top surface of the evaporator during 1 hour evaporation of seawater under 3 sun. To assess the performance of the OPU under extreme salt conditions, different NaCl concentrated brines (3.5 wt%, 10 wt% and 20 wt%) were prepared by dissolving 3.5 g, 10 g and 20 g of NaCl crystals in 100 mL of deionized water, denoted as 3.5B, 10B and 20B, respectively. The mass change and evaporation rates of these four brines in the presence of OPU are shown in Fig. 6c and d. The evaporation rates of the brines are lower compared to those of water and seawater under 1 sun. As the salinity increased, the evaporation rate decreases from 1.49 kg m^{-2} h^{-1} for 3.5B to 1.09 kg m^{-2} h^{-1} for 20B. Furthermore, during the 1 hour evaporation of 20B under 1 sun, no salt growth is observed on the top surface of OPU.

The thermal images were captured during the water evaporation experiments under 1 sun to investigate and measure the temperature of the top surface of the OPU, as shown in Fig. 7a. Prior to each experiment, the OPU was kept on water for some time to make it wet. The top surface temperature of the evaporator reaches 19.7 °C after 1 hour of water evaporation under dark conditions, while the room temperature remains 25 ± 2 °C. The decrease in temperature can be attributed to the energy utilized during water vaporization. Following under 1 sun, the maximum top surface temperature of the evaporator was found to be 37.3 °C with an average value of 33.4 °C after 1 hour of water evaporation experiment. The thermal images also demonstrate that heat is concentrated on the top of the evaporator, resulting in higher water temperature at the top of the beaker. The water temperature at the bottom of the beaker is close to room temperature after 1 hour of water evaporation under 1 sun. Light on–off cycle tests were performed under 1 sun to assess the photothermal response of the OPU during water evaporation, as depicted in Fig. 7b. Initially, the light is kept on for 25 minutes, making the top surface temperature of moist OPU to rise from 22.8 °C (initial temperature of the wet evaporator) to 33.6 °C. Subsequently, the light is turned off for 5 minutes, leading to a gradual decrease in the top surface temperature of the OPU to 25.5 °C. This light on–off test is repeated with a 5 minute interval. While the light is on, the top surface temperature of the OPU exceeds 33 °C within 5 minutes and the temperature never drops below 25.4 °C when the light is

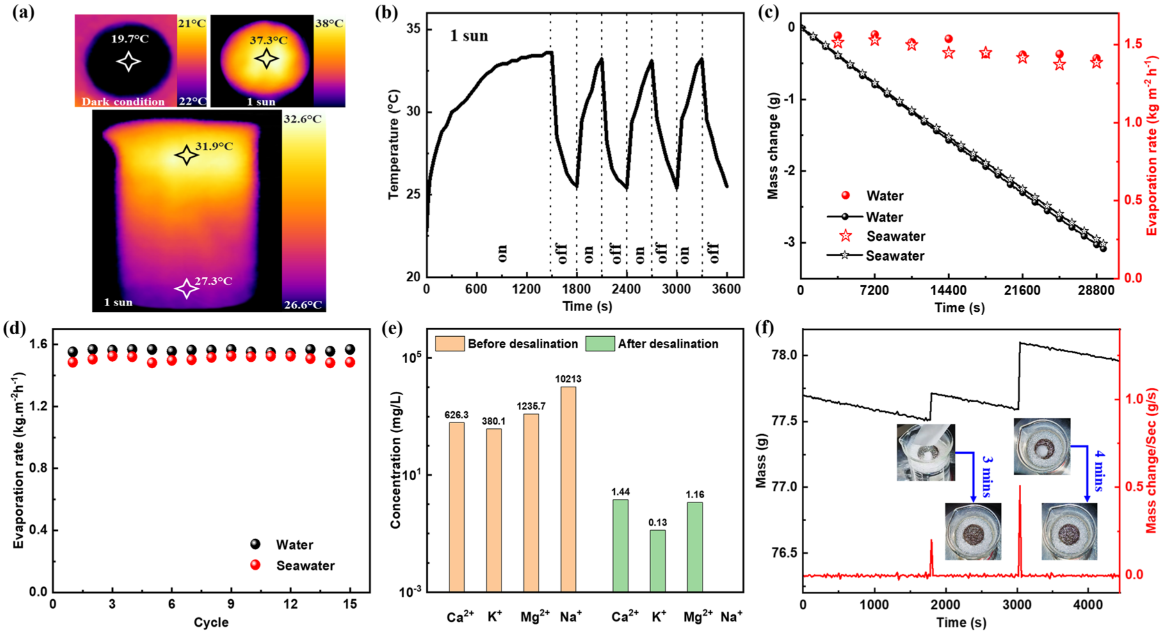

Fig. 7 (a) Thermal images of OPU in the dark, 1 sun and temperature distribution of water at the top and the bottom of the beaker. (b) Light on–off cycle test of OPU under 1 sun with a 5 minute interval. (c) The 8 hour-long evaporation performance for tap water and natural seawater. (d) Cycle tests of evaporating water and seawater under 1 sun for 15 consecutive days. (e) ICP-OES results of concentration of Ca^{2+}, K^+, Mg^{2+} and Na^+ before and after seawater desalination. (f) Salt rejection performance of the OPU.

turned off for 5 minutes. The 8 hours of long evaporation experiments for water and seawater were conducted under 1 sun considering the average daylight irradiation, as observed in Fig. 7c. Initially, the evaporation rate of seawater is high but with time the evaporation rate starts to decrease due to the change in distance between the evaporator and light source (as the water head decreases with time) and the increased salinity of water. The maximum evaporation rate (1.528 kg m^{-2} h^{-1}) is recorded at the 2nd hour and the minimum evaporation rate (1.37 kg m^{-2} h^{-1}) is recorded at the 7th hour. The effect of distance between the light source and evaporator on the evaporation performance of the OPU is further confirmed by the similar trend found during the evaporation of tap water. The maximum evaporation rate (1.57 kg m^{-2} h^{-1}) is recorded at the 2nd hour and the minimum evaporation rate (1.41 kg m^{-2} h^{-1}) is observed at the 8th hour for the tap water sample. In addition, a 13 hour-long experiment was conducted using natural seawater, as shown in Fig. S8.† The resulting data follow the previous trend. The maximum evaporation rate was recorded in the 2nd and 3rd hour which was 1.524 kg m^{-2} h^{-1}. At the 13th hour, the evaporation rate was found to be 1.37 kg m^{-2} h^{-1}. For 2 different days, a similar trend was observed for seawater evaporation under 1 sun in the presence of the same OPU, which confirmed the stability of the prepared evaporator.

Fig. 7d gives the stability tests of the OPU for 15 consecutive days under 1 sun. Each time the beaker is filled with almost the same amount of water to keep the distance between the light source and evaporator the same and each experiment was conducted for at least 1 hour. The evaporation rates of water and seawater in the presence of the OPU do not show any decreasing trend. The small change in evaporation rate found on each day may arise due to the meteorological conditions of the laboratory. For water and sea water, the highest evaporation rates are 1.57 kg m^{-2} h^{-1} and 1.52 kg m^{-2} h^{-1}, while the lowest evaporation rates are 1.54 kg m^{-2} h^{-1} and 1.48 kg m^{-2} h^{-1}, respectively. The standard deviations of evaporation rates are calculated to be 0.8% for water and 5.6% for seawater, indicating the stable performance of the OPU. We use a self-made glass box shown in Fig. S9† to collect the desalinated water for ICP-OES measurement. The concentrations of four cations (Ca^{2+}, K^+, Mg^{2+}, and Na^+) are monitored in both the seawater and the desalinated condensed water. Linear calibration curves are obtained by combining four concentrations of each standard solution combined with a 2.0 vol% HNO_3 solution as the blank sample, as illustrated in Fig. S10.† The standard signals for Ca, K, Mg, and Na are detected at different emission wavelengths (396.8 nm, 769.9 nm, 285.2 nm, and 589.5 nm, respectively). The calibration coefficients for each element's curve exceeded 0.995, indicating the high accuracy of the measurements. The natural seawater is diluted 1000 times to meet the concentration requirement of ICP-OES, while the collected desalinated seawater from the above glass box is used directly without further treatment.

Fig. 7e presents a concentration bar chart comparing the levels of Ca^{2+}, K^+, Mg^{2+}, and Na^+ cations in seawater before and after desalination. The concentrations of Ca^{2+}, K^+, Mg^{2+}, and Na^+ cations in natural seawater are measured at 626 ppm, 380 ppm, 1235 ppm, and 10 213 ppm, respectively. After desalination, the concentrations of the four cations are significantly reduced, reaching 1.438 ppm, 0.129 ppm, and 1.158 ppm for

Ca^{2+}, K^+, and Mg^{2+} cations, respectively. Surprisingly, the concentration of Na^+, which is initially the highest in natural seawater, becomes the lowest after desalination, with almost no traces observed in desalinated water. The concentrations of Ca^{2+}, K^+, and Mg^{2+} in the desalinated water are decreased by three orders of magnitude, while the concentration of Na^+ is decreased by five orders of magnitude. After desalination using the OPU, the concentrations of the four cations remain well below the drinking water standards set by the World Health Organization and Environmental Protection Agency.[55] The organometallic polymer-based evaporator demonstrates great potential for seawater desalination, particularly in the effective removal of Na^+ ions. The salt rejection capability of the OPU was measured and is presented in Fig. 7f. In the experiment, the evaporator was positioned on natural seawater under 1 sun, and the change in mass was recorded every 20 s using an electronic balance system. Around 200 mg of NaCl crystal is directly placed on the top of the evaporator after a 30 minute seawater evaporation period. The salt dissolves back into the sea water within 3 minutes. The evaporation performance is observed for an additional 20 minutes, and then 500 mg of NaCl crystal is placed again on the top surface of the evaporator. Interestingly, the salt dissolves back into the bulk seawater within 4 minutes. This excellent salt rejection capability may be attributed to the porous structure of the OPU. As demonstrated in the SEM image in Fig. S11,† the average pore diameter of the OPU ranges from 94.4 μm to 393.89 μm, facilitating sufficient water transport to the top surface of the OPU, where the salts dissolve and transfer back into the bulk seawater. The addition of salt increases the mass of the beaker as depicted in the inset of Fig. 7f. However, the mass exhibits a decreasing trend over time due to water evaporation. The mass change rate per second remains relatively constant throughout the entire salt dissolution process. Upon completion of the experiment, the salinity of the seawater reached 4.2% as a result of the salt addition and water vaporization.

3 Conclusions

This work presents the synthesis of a new organometallic photothermal polymer, named PffBTPt, by polymerizing the metal complex Pt(N,N)(O,O) with the electron-withdrawing group ffBT-2ET-2DT. The target 1D polymer exhibits a robust and broad absorption capability across the entire solar spectrum in the 300–2500 nm region owing to the synergistic effects of good planarity, extensive conjugation, LLCT and ICT mechanisms. This work is the first successful attempt to achieve a full-solar-spectrum-absorbing polymer by introducing an LLCT-assisted platinum(II) complex in conjunction with the common D–A polymerization strategy. Using the simple drop casting method, an organometallic polymer-based solar evaporator is successfully developed by depositing the PffBTPt polymer onto the PU foam. The surface temperature of the OPU can rapidly rise to nearly its highest value of 66.4 °C within 1 minute under 1 sun radiation, significantly exceeding the 36.5 °C of the PU substrate. The water evaporation rate and efficiency of the OPU can reach up to 85.6% and 1.57 kg m^{-2} h^{-1}, respectively, under 1 sun, comparable to the reported studies. These parameters demonstrate excellent maintenance even after the 13 hour-long test or 15 consecutive cycles, indicating the good operational stability of the evaporator. fs-TA spectra reveal that the light-to-thermal conversion is attributed to the effective non-radiative relaxation of PffBTPt. Moreover, the prepared solar evaporator exhibits excellent salt rejection capability and seawater desalination performance, particularly achieving a five-order of magnitude decrease of Na^+ concentration in the desalinated seawater. This work introduces a new idea in the molecular design to develop effective organometallic photothermal materials by incorporating an appropriate metal complex into the polymer backbone. It demonstrates the tremendous potential of organometallic polymers for simultaneous clean water production and seawater desalination, making an important advancement in the ISSG field.

Author contributions

Miao Zhang: conceptualization, investigation, visualization, writing-original draft, funding acquisition; Md. Nahian Al Subri Ivan: data curation, investigation, visualization, writing-original draft; Yingjie Sun: methodology; Zikang Li: software; Shuvra Saha: data curation; Safayet Ahmed: data curation; Huiying Liu: data curation, formal analysis; Yidi Wang: data curation, formal analysis; Yuen Hong Tsang: funding acquisition, resources, supervision, writing-review and editing; Wai-Yeung Wong: funding acquisition, project administration, resources, supervision, writing-review and editing.

Conflicts of interest

The authors declare no conflict of interest.

Acknowledgements

This work was supported by the National Natural Science Foundation of China (62205276 and 52073242), the Hong Kong Research Grants Council (PolyU 15307321), RGC Senior Research Fellowship Scheme (SRFS2021-5S01), Research Institute for Smart Energy (CDAQ), Ms. Clarea Au for the Endowed Professorship in Energy (847S), the Guangdong International Science and Technology Cooperation Foundation (2020A0505100002), Photonic Research Institute, the Hong Kong Polytechnic University (1-BD51, 1-CD6V, 1-CD6F, 1-WZ5J and 1-CD8V), Research Institute for Advanced Manufacturing (RIAM) and the Innovation and Technology Fund, Hong Kong, China (GHP/040/19SZ). The authors also appreciate the technical support by Ceshigo Research service (**https://www.ceshigou.com**) on transient absorption characterization.

Notes and references

1 H. W. Liu, B. C. Chen, Y. L. Chen, M. N. Zhou, F. W. Tian, Y. Z. Li, J. J. Jiang and W. T. Zhai, *Adv. Mater.*, 2023, **35**, 2301596.

2 Z. H. Wu, D. Sun, C. C. Shi, S. Chen, S. H. Tang, Y. K. Li, C. Z. Yan, Y. S. Shi and B. Su, *Adv. Funct. Mater.*, 2023, **33**, 2304897.

3 C. J. Xu, M. Y. Gao, X. X. Yu, J. Y. Zhang, Y. H. Cheng and M. F. Zhu, *Nanomicro Lett.*, 2023, **15**, 64.

4 S. H. Choi, *Desalination*, 2016, **398**, 64–76.

5 X. C. Zhou, Z. X. Wang, R. Epsztein, C. Zhan, W. L. Li, J. D. Fortner, T. A. Pham, J. H. Kim and M. Elimelech, *Sci. Adv.*, 2020, **6**, eabd9045.

6 N. Xu, J. Li, C. Finnerty, Y. Song, L. Zhou, B. Zhu, P. Wang, B. Mi and J. Zhu, *Nat. Water*, 2023, **1**, 494–501.

7 Y. W. Yang, H. X. Feng, W. X. Que, Y. Qiu, Y. Q. Li, L. Guo and Q. Li, *Adv. Funct. Mater.*, 2023, **33**, 2210972.

8 X. Zhao, X. T. Meng, H. Q. Zou, Z. H. Wang, Y. D. Du, Y. Shao, J. Qi and J. S. Qiu, *Adv. Funct. Mater.*, 2023, **33**, 2209207.

9 M. N. A. Ivan, A. M. Saleque, S. Ahmed, Z. L. Guo, D. Zu, L. L. Xu, T. I. Alam, S. U. Hani and Y. H. Tsang, *J. Mater. Chem. A*, 2023, **11**, 3961–3974.

10 F. Zhao, Y. H. Guo, X. Y. Zhou, W. Shi and G. H. Yu, *Nat. Rev. Mater.*, 2020, **5**, 388–401.

11 A. M. Saleque, N. Nowshin, M. N. A. Ivan, S. Ahmed and Y. H. Tsang, *Sol. RRL*, 2022, **6**, 2100986.

12 Z. M. Huang, Y. Liu, S. L. Li, C. S. Lee and X. H. Zhang, *Small Methods*, 2022, **6**, 2200835.

13 Y. Z. Liu, Z. P. Liu, Q. C. Huang, X. C. Liang, X. C. Zhou, H. D. Fu, Q. X. Wu, J. M. Zhang and W. Xie, *J. Mater. Chem. A*, 2019, **7**, 2581–2588.

14 M. W. Ji, H. C. Liu, M. S. Cheng, L. Huang, G. Yang, F. Bao, G. C. Huang, Y. K. Huang, Y. Z. Hu, G. T. Cong, J. L. Yu, C. Z. Zhu and J. Xu, *J. Phys. Chem. C*, 2022, **126**, 2454–2462.

15 K. Goharshadi, S. A. Sajjadi, E. K. Goharshadi and R. Mehrkhah, *Mater. Res. Bull.*, 2022, **154**, 111916.

16 Y. D. Kuang, C. J. Chen, S. M. He, E. M. Hitz, Y. L. Wang, W. T. Gan, R. Y. Mi and L. B. Hu, *Adv. Mater.*, 2019, **31**, 1900498.

17 Y. M. Li, Y. Y. Shi, H. W. Wang, T. F. Liu, X. W. Zheng, S. M. Gao and J. Lu, *Carbon Energy*, 2023, **e331**, 1–42.

18 A. M. Saleque, M. N. A. Ivan, S. Ahmed and Y. H. Tsang, *Chem. Eng. J.*, 2023, **458**, 141430.

19 X. L. Yan, S. Z. Lyu, X. Q. Xu, W. B. Chen, P. N. Shang, Z. F. Yang, G. Zhang, W. H. Chen, Y. P. Wang and L. Chen, *Angew. Chem., Int. Ed.*, 2022, **61**, e202201900.

20 X. H. Ye, L. H. Chung, K. D. Li, S. L. Zheng, Y. L. Wong, Z. H. Feng, Y. H. He, D. D. Chu, Z. T. Xu, L. Yu and J. He, *Nat. Commun.*, 2022, **13**, 6116.

21 Q. B. Zhao, Y. Q. Wan, F. Chang, Y. F. Wang, H. K. Jiang, L. Jiang, X. Y. Zhang and N. Ma, *Desalination*, 2022, **527**, 115581.

22 Z. J. Xie, J. T. Zhu and L. B. Zhang, *ACS Appl. Mater. Interfaces*, 2021, **13**, 9027–9035.

23 Z. Wang, Y. T. Yan, X. P. Shen, C. D. Jin, Q. F. Sun and H. Q. Li, *J. Mater. Chem. A*, 2019, **7**, 20706–20712.

24 S. Wang, Y. K. Fan, F. Wang, Y. N. Su, X. Zhou, Z. Q. Zhu, H. X. Sun, W. D. Liang and A. Li, *Desalination*, 2021, **505**, 114982.

25 Y. Zhou, T. Kurosawa, W. Ma, Y. K. Guo, L. Fang, K. Vandewal, Y. Diao, C. G. Wang, Q. F. Yan, J. Reinspach, J. G. Mei, A. L. Appleton, G. I. Koleilat, Y. L. Gao, S. C. B. Mannsfeld, A. Salleo, H. Ade, D. H. Zhao and Z. N. Bao, *Adv. Mater.*, 2014, **26**, 3767–3772.

26 L. Gao, Z. G. Zhang, L. W. Xue, J. Min, J. Q. Zhang, Z. X. Wei and Y. F. Li, *Adv. Mater.*, 2016, **28**, 1884–1890.

27 Q. An, J. Wang, W. Gao, X. Ma, Z. Hu, J. Gao, C. Xu, M. Hao, X. Zhang, C. Yang and F. Zhang, *Sci. Bull.*, 2020, **65**, 538–545.

28 G. Y. Chen, J. M. Sun, Q. Peng, Q. Sun, G. Wang, Y. J. Cai, X. G. Gu, Z. G. Shuai and B. Z. Tang, *Adv. Mater.*, 2020, **32**, 1908537.

29 S. P. Zhang, M. Zhang, X. L. Wang, C. Y. Xu, W. J. Xu, J. H. Gao, J. Wang, W. Y. Wong, J. H. Son, S. Y. Jeong, H. Y. Woo and F. J. Zhang, *Sustainable Energy Fuels*, 2021, **5**, 5825–5832.

30 Z. Liu, M. Zhang, L. Zhang, S. Y. Jeong, S. Geng, H. Y. Woo, J. Zhang, F. Zhang and X. Ma, *Chem. Eng. J.*, 2023, **471**, 144711.

31 W. Xu, M. Zhang, X. Ma, X. Zhu, S. Y. Jeong, H. Y. Woo, J. Zhang, W. Du, J. Wang, X. Liu and F. Zhang, *Adv. Funct. Mater.*, 2023, **33**, 2215204.

32 V. W.-W. Yam, A. K.-W. Chan and E. Y.-H. Hong, *Nat. Rev. Chem.*, 2020, **4**, 528–541.

33 N. Sinha and O. S. Wenger, *J. Am. Chem. Soc.*, 2023, **145**, 4903–4920.

34 Y. H. Sun, C. Y. Zhu, S. Q. Liu, W. T. Wang, X. Chen, G. J. Zhou, X. L. Yang and W. Y. Wong, *Chem. Eng. J.*, 2022, **449**, 137457.

35 H. Lian, X. Z. Cheng, H. T. Hao, J. B. Han, M. T. Lau, Z. K. Li, Z. Zhou, Q. C. Dong and W. Y. Wong, *Chem. Soc. Rev.*, 2022, **51**, 1926–1982.

36 D. N. Tritton, F. K. Tang, G. B. Bodedla, F. W. Lee, C. S. Kwan, K. C. F. Leung, X. J. Zhu and W. Y. Wong, *Coord. Chem. Rev.*, 2022, **459**, 214390.

37 L. L. Xu, J. B. Sun, T. H. Tang, H. Y. Zhang, M. Z. Sun, J. Q. Zhang, J. H. Li, B. L. Huang, Z. P. Wang, Z. Xie and W. Y. Wong, *Angew. Chem., Int. Ed.*, 2021, **60**, 11326–11334.

38 M. Zhang, X. L. Ma, H. Y. Zhang, L. Z. Zhu, L. L. Xu, F. J. Zhang, C. S. Tsang, L. Y. S. Lee, H. Y. Woo, Z. C. He and W. Y. Wong, *Chem. Eng. J.*, 2022, **430**, 132832.

39 M. Zhang, F. Zhang, Q. An, Q. Sun, W. Wang, J. Zhang and W. Tang, *Nano Energy*, 2016, **22**, 241–254.

40 J. Marques dos Santos, M. Neophytou, A. Wiles, C. T. Howells, R. S. Ashraf, I. McCulloch and G. Cooke, *Dyes Pigm.*, 2021, **188**, 109152.

41 H. W. Hu, K. Jiang, G. F. Yang, J. Liu, Z. K. Li, H. R. Lin, Y. H. Liu, J. B. Zhao, J. Zhang, F. Huang, Y. Q. Qu, W. Ma and H. Yan, *J. Am. Chem. Soc.*, 2015, **137**, 14149–14157.

42 J. B. Zhao, Y. K. Li, G. F. Yang, K. Jiang, H. R. Lin, H. Ade, W. Ma and H. Yan, *Nat. Energy*, 2016, **1**, 15027.

43 T. Lu and F. Chen, *J. Comput. Chem.*, 2012, **33**, 580–592.

44 B. Sarkar, R. Hubner, R. Pattacini and I. Hartenbach, *Dalton Trans.*, 2009, **24**, 4653–4655.

45 G. K. Rauth, S. Pal, D. Das, C. Sinha, A. M. Z. Slawin and J. D. Woollins, *Polyhedron*, 2001, **20**, 363–372.

46 H. Yu, S. W. Luo, R. Sun, I. Angunawela, Z. Y. Qi, Z. X. Peng, W. T. Zhou, H. Han, R. Wei, M. G. Pan, A. M. H. Cheung,

D. H. Zhao, J. Q. Zhang, H. Ade, J. Min and H. Yan, *Adv. Funct. Mater.*, 2021, **31**, 2100791.

47 L. Zhu, M. Zhang, J. Xu, C. Li, J. Yan, G. Zhou, W. Zhong, T. Hao, J. Song, X. Xue, Z. Zhou, R. Zeng, H. Zhu, C.-C. Chen, R. C. I. MacKenzie, Y. Zou, J. Nelson, Y. Zhang, Y. Sun and F. Liu, *Nat. Mater.*, 2022, **21**, 656–663.

48 K. Basuroy, J. D. Velazquez-Garcia, D. Storozhuk, R. Henning, D. J. Gosztola, S. T. Veedu and S. Techert, *J. Chem. Phys.*, 2023, **158**, 054304.

49 Y. Y. Shao, T. Lu, M. J. Li and W. C. Lu, *New J. Chem.*, 2022, **46**, 3370–3382.

50 S. Q. Li, Y. Deng, J. Huang, P. Wang, G. L. Liu and H. L. Xie, *Aggregate*, 2023, **4**, e371.

51 W. B. Hu, X. F. Miao, H. J. Tao, A. Baev, C. Ren, Q. L. Fan, T. C. He, W. Huang and P. N. Prasad, *ACS Nano*, 2019, **13**, 12006–12014.

52 C. H. Xu, R. Q. Ye, H. C. Shen, J. W. Y. Lam, Z. Zhao and B. Z. Tang, *Angew. Chem., Int. Ed.*, 2022, **61**, e202204604.

53 Y. Yuan, C. Dong, J. Gu, Q. Liu, J. Xu, C. Zhou, G. Song, W. Chen, L. Yao and D. Zhang, *Adv. Mater.*, 2020, **32**, 1907975.

54 M. N. A. S. Ivan, S. Saha, A. M. Saleque, S. Ahmed, A. K. Thakur, G. Bai, Z. Miao, R. Saidur and Y. H. Tsang, *Nano Energy*, 2024, **120**, 109176.

55 S. H. Wu, G. P. Xiong, H. C. Yang, B. Y. Gong, Y. K. Tian, C. X. Xu, Y. Wang, T. Fisher, J. H. Yan, K. F. Cen, T. F. Luo, X. Tu, Z. Bo and K. Ostrikov, *Adv. Energy Mater.*, 2019, **9**, 1901286.